CRYSTAL GROWTH & DESIGN

pubs.acs.org/crystal

Article

Spatiotemporal Distribution of Calcium Oxalate Crystals in a Microchannel

Paszkál Papp, Samantha Bourg, Michael Emmanuel, Ágota Tóth, Ali Abou-Hassan,* and Dezső Horváth*

Cite This: *Cryst. Growth Des.* 2023, 23, 8116−8123

Read Online

ACCESS | Metrics & More | Article Recommendations

ABSTRACT: The formation of crystals under physicochemical and flow dynamic conditions in constrained dimensions is ubiquitous in nature and of great interest to different disciplines in science. In this report, using a physicochemical approach, we investigated the spatiotemporal precipitation of calcium oxalate (CaOx) crystals, the most common chemical compound found in kidney stones, at the dynamic interface generated by the interdiffusion of oxalate and calcium ions in a microchannel. Spatiotemporal crystal habit distributions were mapped and analyzed using scanning electron microscopy, and their formation was correlated to a numerical model that accounts for supersaturation and gravity. We show that while monohydrated CaOx crystals are the most frequent with random distribution in the channel, the dihydrated CaOx phase crystals are mainly formed at the contact line between oxalate and calcium at the oxalate side, where gradients are large and supersaturation is low. In addition, the size of the crystals correlates well with the supersaturation with increasing monodispersity over time. These results are supported by the numerical model. The simulations also show that nucleation can occur everywhere in the channel; however, with time, nucleation is limited to the upper level of the channel, while crystals on the bottom continue to grow from the reactants.

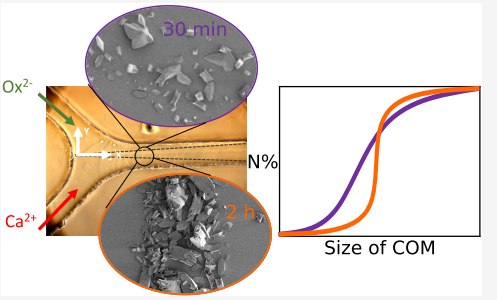

INTRODUCTION

The growth of crystals under physicochemical and flow dynamic conditions is a hot topic nowadays in the field of chemistry and materials science.[1−5] Kidney stones are among other biomaterials that form out-of-equilibrium dynamic conditions in constrained channels in kidneys with medical and societal consequences.[6] Kidney stones are composed of organic and inorganic species, among them and in majority calcium oxalate crystals.[7] Reproducing, even partially, the precipitation of calcium oxalate (CaOx) crystals in confined channels is interesting for several disciplines including physical chemistry, materials science, and medicine.[8−10]

Microfluidic channels are microsystems that offer the opportunity to reproduce and mimic the dimensions and hydrodynamic conditions encountered, for example, in the tubular part of nephrons where calcium oxalate crystals can nucleate and form.[8] Previous work by our group[11,12] allowed us to investigate in a microfluidic device the effect of diffusive mixing on the crystalline phases of calcium oxalate precipitating at miscible liquid−liquid dynamical interfaces in physiological conditions (concentrations and flow rates). The results were discussed and confronted by medical observations. In addition, due to the reversibility of the system, it was possible to image and characterize using different multiscale techniques the precipitated CaOx crystals. Kinetic studies on a single CaOx crystal were also possible using this system and permitted one to acquire single-crystal growth kinetics by tracking the size and morphology using light microscopy.

In continuous microfluidics, the flow is laminar, so one may assume that space can be converted to time. The space-time equivalence has been exploited by several groups for kinetic studies in different problems including nanomaterial synthesis or crystal formation.[13−16] In the case of CaOx formation, spatial analysis of crystals in the direction of the flow at different positions of the channel may reflect their evolution with time during their formation by interdiffusive mixing and may allow us consequently to better describe the dynamics of growth in the channel as well as the habits of the crystal's formation.

In this study, following our previous reports, and in a physicochemical approach, we mapped the spatiotemporal distribution of CaOx crystals inside a 100 × 100 μm^2 cross section microchannel of similar dimensions to the collective duct in nephrons. The precipitation was induced under the comixing of supersaturated calcium and oxalate aqueous

Received: July 14, 2023
Revised: September 4, 2023
Published: October 2, 2023

https://doi.org/10.1021/acs.cgd.3c00839
Cryst. Growth Des. 2023, 23, 8116−8123

solutions to mimic the pathological conditions for CaOx kidney stone formation. The precipitation behavior of CaOx crystals was studied, and the crystals were analyzed (size, morphology, and position in the channel). The habits of the crystal were examined, taking into account the diffusive mixing and the supersaturation. Finally, a theoretical model was developed and confronted with the experimental results.

EXPERIMENTAL SECTION

Calcium chloride and sodium oxalate salts were purchased from Merck and Prolabo, respectively, and used as received. Oxalate ($[Ox^{2-}]$ = 0.4 mM) and calcium ion ($[Ca^{2+}]$ = 12.0 mM) solutions were prepared and used as they correspond to moderate hyperoxaluria ($[Ox^{2-}]$ = 0.4 mM) and pathological hypercalciuria ($[Ca^{2+}]$ = 12.0 mM), respectively. A Y-shaped reversible microfluidic channel with a cross section of 100 × 100 μm^2 was produced using a standard soft lithographic process as described by us previously.[12] Each solution was injected at a flow rate of 1 μL/min per channel with a KD Scientific syringe pump. The phases and morphologies of CaOx crystals were identified by scanning electron microscopy (Hitachi S-3400). The size of calcium oxalate monohydrate crystals formed in the microchannel is determined by measuring the lengths of the longer side of the crystals on the microscopic images in `ImageJ` via the region of interest (ROI) manager tool. With this feature, lines are manually selected on each of the crystals. A list containing the lengths of all of the lines is generated and then further analyzed to display the particle size distribution. Overall, 910 particles were analyzed, 203 particles were identified 30 min after the commencement of reaction injection, and the remaining 707 particles were obtained 2 h after the injection.

THEORETICAL SECTION

In order to gain a deeper understanding of the spatiotemporal distribution of calcium oxalate, a (3D) numerical model has been developed. Experimentally, two miscible fluids, $CaCl_2$ and $Na_2C_2O_4$ solutions, flow into a microfluidic channel. Upon contact, a precipitation reaction takes place, and CaC_2O_4 solid particles are formed, resulting in a solid−liquid two-phase system.

The fluid propagates laminarly in the channel, as the Reynolds number corresponding to the flow regime is Re = 0.33. The flow field is described by the Navier−Stokes equation for incompressible fluids ($\nabla\cdot\vec{u} = 0$) as

$$\frac{\partial \vec{u}}{\partial t} + (\vec{u}\cdot\nabla)\vec{u} = \frac{\eta}{\rho_0}\nabla^2\vec{u} - \frac{\nabla p}{\rho_0} + \frac{\rho}{\rho_0}\vec{g} + \sum \vec{F}_j \tag{1}$$

where $\vec{u}$ is the flow velocity, p is the pressure, η = 1 mPas is the dynamic viscosity of the liquid, ρ is the density of the solutions, ρ_0 is that of the solvent, and $\sum \vec{F}_j$ is the force per volume originating from the presence of the solid particles. The interaction between the solid particles and the fluid medium was modeled by using the two-way coupling approach. The drag force caused by the jth particles is calculated as

$$\vec{F}_j = \frac{3\rho C_D|\vec{u}_{p,j} - \vec{u}|}{4\rho_p d_j} \tag{2}$$

where $\vec{u}_{p,j}$ is the velocity, d_j is the diameter, ρ_p is the density of the jth solid spherical particle, and C_D is the drag coefficient.[24] Boussinesq approximation can be applied because dilute solutions have been used in the experiments. Therefore, the solution density appears only in the term containing the gravitational acceleration in eq 1. In all other terms, ρ is replaced with ρ_0, the density of the solvent (water). At these concentrations, the solution density is a linear function of the composition according to

$$\rho = \rho_0 + \sum \rho_i c_i \tag{3}$$

where ρ_i is the density contribution of species i with concentration c_i.

In our model, the precipitation reaction is divided into two steps: a homogeneous one and a heterogeneous one. The first reaction between calcium chloride and sodium oxalate

$$CaCl_{2(aq)} + Na_2C_2O_{4(aq)} \rightarrow CaC_2O_{4(aq)} + 2NaCl_{(aq)} \tag{4}$$

only takes place if the condition

$$Q \equiv [Ca^{2+}_{(aq)}][C_2O^{2-}_{4(aq)}] > K_{sp} \tag{5}$$

is fulfilled, where $K_{sp} = 2.32 \times 10^{-9}$ is the solubility product;[17] thus, the solution is supersaturated. The formed $CaC_2O_{4(aq)}$ is treated as a colloidal solute in the liquid phase, from which the solid $CaC_2O_{4(s)}$ precipitate is produced in the second, heterogeneous reaction of

$$CaC_2O_{4(aq)} \rightarrow CaC_2O_{4(s)} \tag{6}$$

In the calculations, the position and size of each solid particle formed are monitored. At this Reynolds number, the effect of the particle shape is negligible on the flow field; therefore, spherical particles are considered. Since the supersaturation in the system is dominant, the dissolution of the precipitate can be neglected.[12]

The temporal change of the homogeneous species ($CaCl_2$, $Na_2C_2O_4$, NaCl, CaC_2O_4) is described by the component balance equation

$$\frac{\partial c_i}{\partial t} + (\vec{u}\cdot\nabla)c_i = D\nabla^2 c_i + \nu_i r_s \tag{7}$$

where the second term on the left side of the equation is the contribution of advection, while on the right side, the diffusion and kinetic source terms are presented, with ν_i being the stoichiometric coefficient. We assume that the components have the same $D = 2 \times 10^{-9}$ m^2/s diffusion coefficient. The reaction rate (r_s) of the solid particle formation in eq 7 incorporates the nucleation (r_n) and growth rate (r_g) of the particles as

$$r_s = r_n + r_g = \left(k_n + k_g \sum_j d_j^2\right)(Q - K_{sp}) \tag{8}$$

where k_n and k_g are the rate coefficients for nucleation and growth, respectively, as dissolution and phase change are neglected on this time scale. In addition to supersaturation, the growth rate is proportional to the surface area of solid particles.[12,18,19]

If the solution is supersaturated, $CaC_2O_{4(aq)}$ will accumulate in a ΔV volume of the unit cell unless a sufficient amount is formed according to

$$\Delta n_n = \frac{k_n}{k_n + k_g \sum_j d_j^2} r_s \Delta t \Delta V \tag{9}$$

that can allow the generation of a particle with

https://doi.org/10.1021/acs.cgd.3c00839
Cryst. Growth Des. 2023, 23, 8116−8123

$$d_{new} = \left(\frac{6M\Delta n_n}{\rho_p \pi}\right)^{1/3} > 1\ \mu m \tag{10}$$

where M is the molar mass of CaC_2O_4 and 1 μm is the upper limit of the colloidal range. The iteration time step ($\Delta t = 10^{-4}$ s) is set to be sufficiently small so that a maximum of one new particle can appear in a volume cell. The generated particle is positioned randomly within the volume cell.

The size of the jth particle existing in the volume cell is increased at each iteration step according to

$$\Delta d_j = \left(d_j^3 + \frac{6M\Delta n_{g,j}}{\pi\rho_p}\frac{d_j^2}{\sum_j d_j^2}\right)^{1/3} - d_j \tag{11}$$

where $\Delta n_{g,j}$ equals to

$$\Delta n_{g,j} = \frac{k_g d_j^2}{k_n + k_g \sum_j d_j^2} r_s \Delta t \Delta V \tag{12}$$

In order to solve eqs 1 and 7, the OpenFoam software package[20] was used with the PISO algorithm.[21] The spatial discretization was performed by applying the finite volume element method. The microfluidic reactor was represented with a 25 × 0.1 × 0.1 mm^3 channel (200 × 10 × 5 cells) with two inlets arranged in a T-shape. At the inlets and outlets, fixed values were set for flow rate q = 1 μL/min and for initial concentrations $[Na_2C_2O_4]_0$ = 0.4 mmol/L and $[CaCl_2]_0$ = 12 mmol/L. At the walls, the `No Slip` boundary condition was used for the velocity and `Zero Gradient` for the concentration fields. The differential equations were solved using Euler's method. To describe the trajectories of the solid particles, Lagrangian particle tracking was utilized. The reaction rate constants for nucleation k_n = 10 m^3/(smol) and k_g = 10^{-13} m/(smol) were set to match the experimental observations.

RESULTS AND DISCUSSION

After injection of the reactants for different times (30 min and 2 h), the microfluidic channel was unsealed, and the precipitated crystals in the interdiffusion zone at different distances from the zone of confluence (X = 0 μm), defined in Table 1, were imaged using scanning electron microscopy (SEM). The majority of crystals formed are twins or prismatic structures, a morphology associated with monohydrated CaOx crystals (COM; Figure 1).

Table 1. Bin Definitions with Reference to the Distance from the Confluence along the Channel

label	range (μm)	label	range (μm)
H_1	$0 < X \leq 75$	H_2	$75 < X \leq 150$
H_3	$150 < X \leq 225$	H_4	$225 < X \leq 300$
H_5	$300 < X \leq 375$	H_6	$375 < X \leq 450$
H_7	$450 < X \leq 525$	H_8	$525 < X \leq 600$
H_9	$600 < X \leq 675$	H_{10}	$675 < X \leq 752$

Occasional bipyramid structures relative to the dihydrated CaOx (COD), indicated by a white asterisk in Figure 1, phase were observed. Interestingly, COD crystals appear mainly at the contact line between oxalate and calcium on the oxalate side where gradients are high, and supersaturation, defined as SS = $[Ca^{2+}][Ox^{2-}]/K_{sp}$, is significantly less than that in the center of the zone (Figure 1(e,f)). These results suggest that the thermodynamically unstable phase COD is promoted by steep gradients.

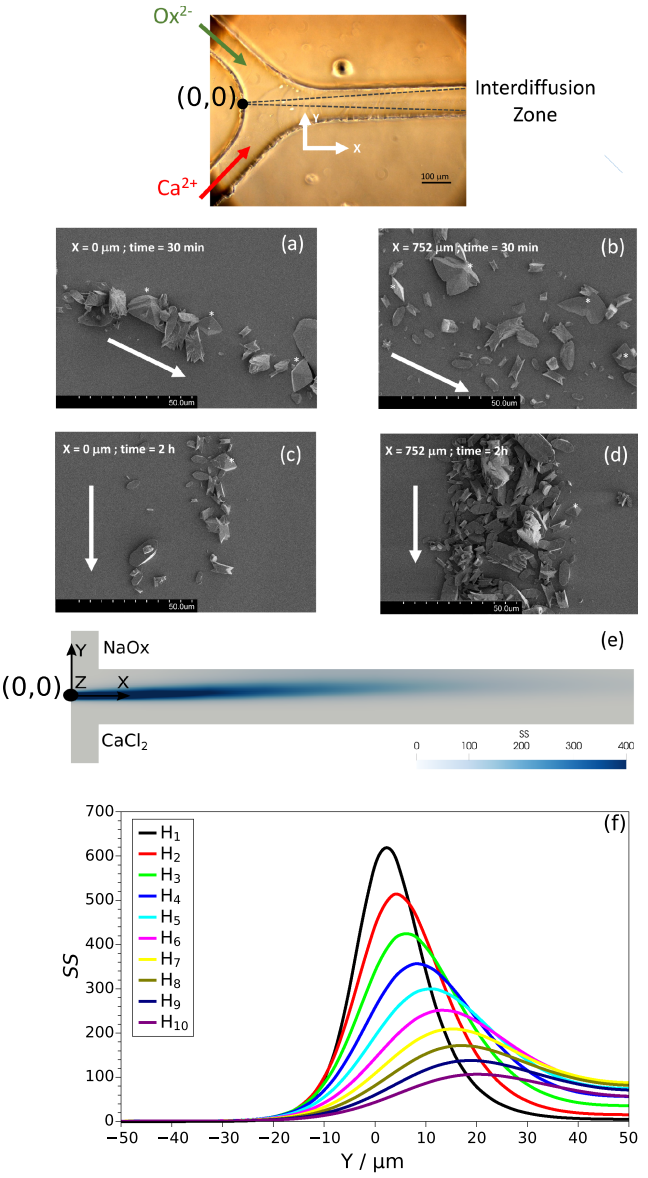

Figure 1. Light microscopy image of the microfluidic channel used in this study. The white arrow indicates the direction of the flow after injection of Ca^{2+} and Ox^{2-} solutions. The gravitational force acts in the $-Z$ direction. Calcium oxalate crystals are formed due to mixing in the interdiffusion zone at different portions of the microchannel: after 30 min of injecting the reactants near the zone of confluence (X = 0 μm) and at 752 μm after 30 min (a, b) and after 2 h of injecting the reactants (c, d), respectively. COD crystals are indicated with a white asterisk. Simulated supersaturation (SS) 2D profile in the microchannel (e) and plot profiles of the SS across different positions of the channel (f).

At 30 min, images of the crystals obtained near the inlet (Figure 1(a)) showed a small size in agreement with a highly supersaturated region where nucleation is easily initiated, resulting in a multitude of smaller crystals, similar to magnesium hydroxide precipitation.[22] As the reactants diffuse into each other, the supersaturation gradually decreases (Figure 1(a,c)),[23] thus yielding fewer crystals of larger and

https://doi.org/10.1021/acs.cgd.3c00839
Cryst. Growth Des. 2023, 23, 8116−8123

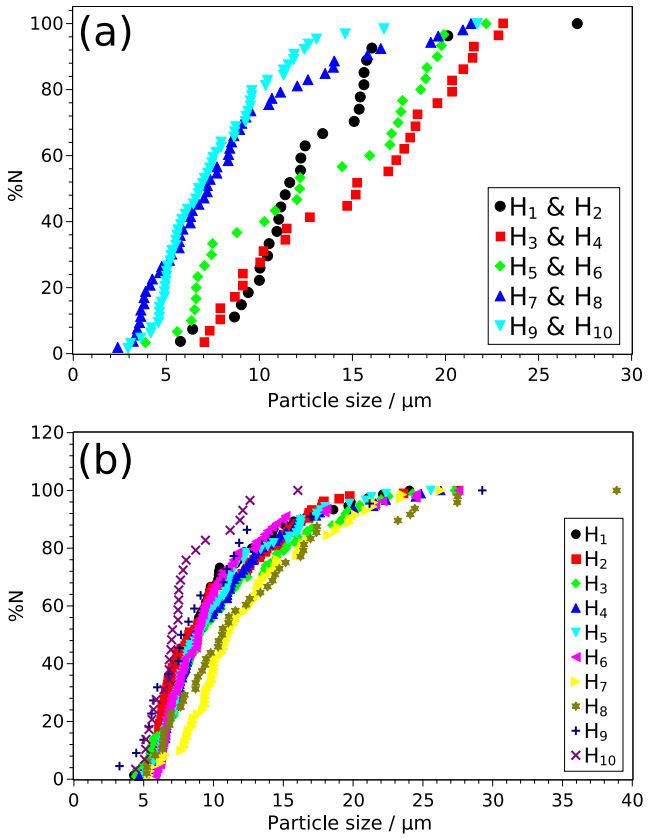

Figure 2. Cumulative particle size distribution of calcium oxalate monohydrate crystals formed in microchannels. Different colors indicate particles analyzed at a given distance from the point of confluence after injecting the reactants for 30 min (a) and 2 h (b).

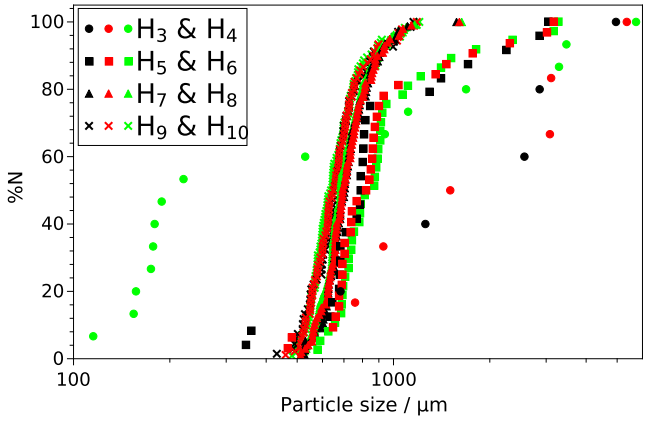

Figure 3. Calculated cumulative particle size distribution at various distances from the point of confluence at t = 1300 (black), 1600 (red), and 1900 s (green).

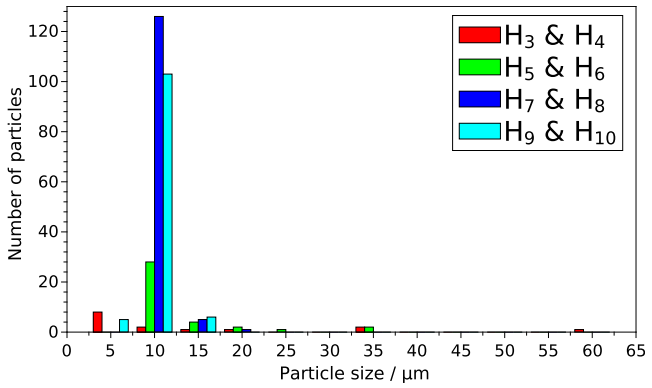

Figure 4. Histogram of the calculated particle size distribution at various distances from the point of confluence at t = 1900 s.

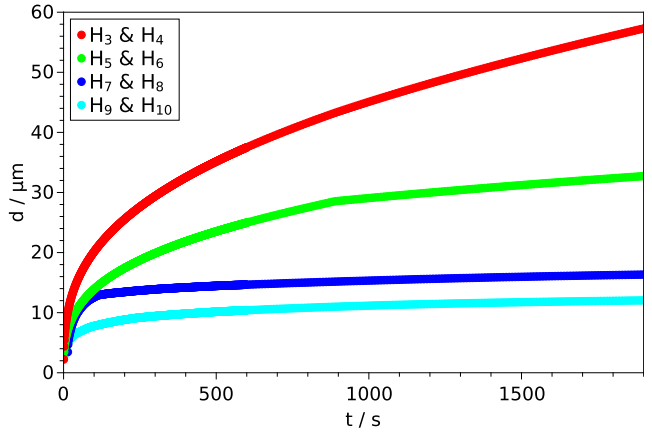

Figure 5. Growth of the largest particles from each zone.

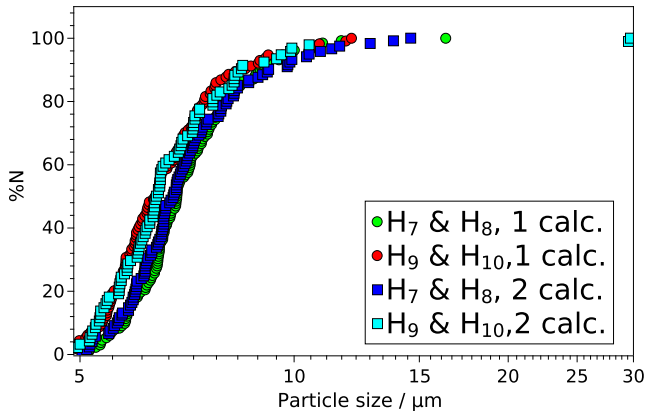

Figure 6. Result of two calculations with the same parameters. The cumulative distribution of the zones 450−600 μm and 600−750 μm is presented for both calculations.

different sizes. Near the outlet, the reactants are almost completely mixed, giving rise to crystals of relatively similar sizes, and the clear contact line seen at the inlet vanishes (Figure 1(b)).

It can be seen from Figures 1(c) and 2(a) that at regions farther from the point of confluence after 30 min of injecting the reactants, the crystals are relatively small and uniform in size. Near the inlet, the crystal size distribution is comparatively high. Two hours after flowing the reactants into the microchannels (Figures 1(d) and 2(b)), the crystals appear to be of similar sizes and their distribution is narrow compared to crystals obtained 30 min after reactants' injection.

During the calculations, the size distribution of particles was investigated both spatially and temporally. Although many particles sedimented, the flow along the tube was dominant (u_x/u_z = 100:1); therefore, most of the particles drifted out of the reactor. In order to support the experiments, the initial part of the microfluidic channel, after the point of confluence, was divided into five 150 μm long segments. The number of the particles and their sizes were determined at each of these bins at three different times. The cumulative particle size

https://doi.org/10.1021/acs.cgd.3c00839
Cryst. Growth Des. 2023, 23, 8116−8123

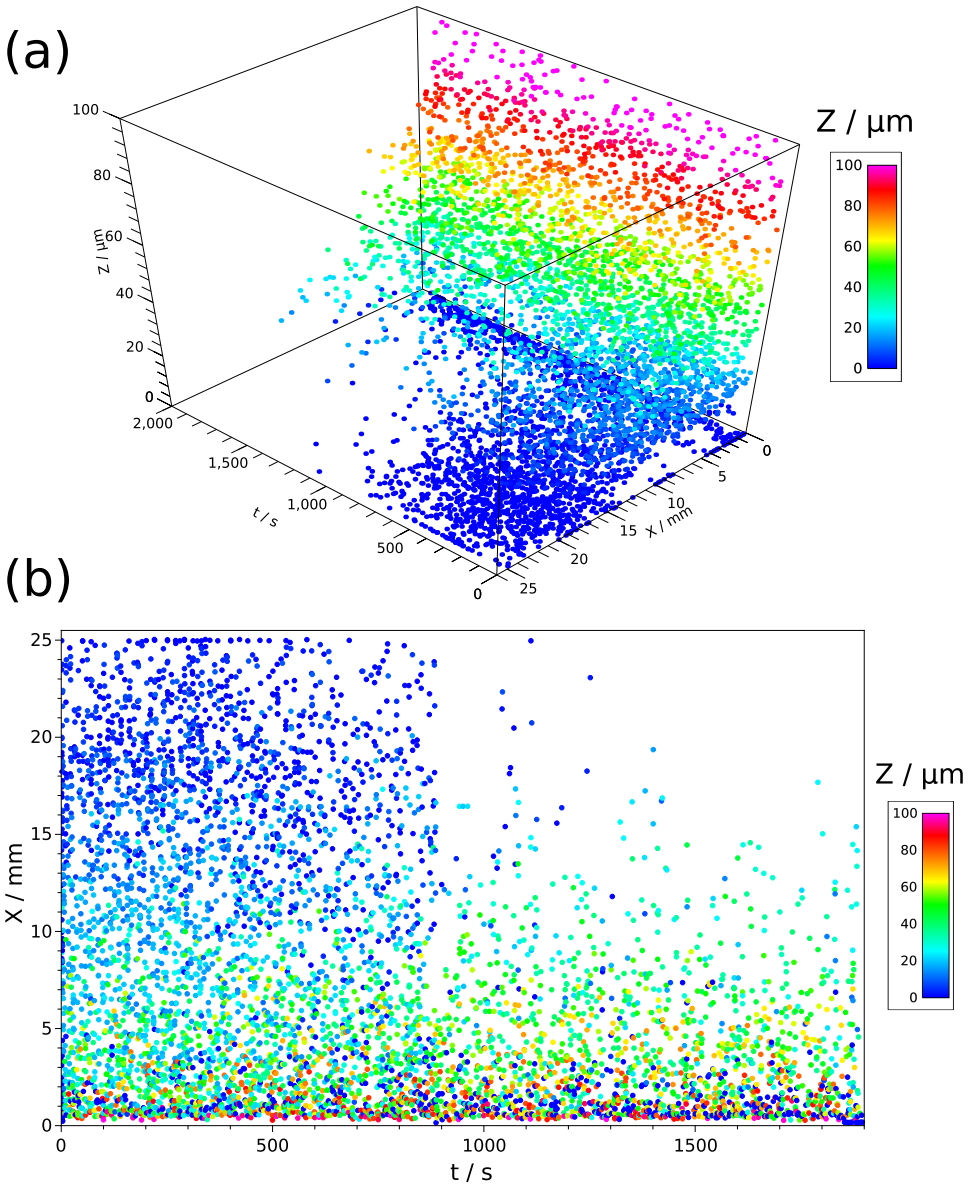

Figure 7. Time and location of nucleation sites for particles that sediment in the channel (a) and its 2D presentation (b).

distribution in Figure 3 indicates that the size of the particles is larger and closer to the inlets; moreover, they grow fiercely compared to those situated further away. The slope of the curves increases toward the outlet; thus, further away from the point of confluence, the particle size distribution is more monodisperse. Moreover, the slopes do not vary significantly over time, so the dispersity of the bins is constant throughout the numerical experiments. The differences among the bins, regarding the final particle size and the growth rate, become less significant further away from the inlet.

The number of particles closer to the outlet is greater (see Figure 4), which explains the position-dependent growth rate and size of the particles. In crowded regions, the amount of substance responsible for growth is distributed among many particles; thus, their growth rate is less and they reach smaller sizes than the isolated particles at the front.

Therefore, the largest particle in each bin was chosen, and its growth was monitored. Figure 5 confirms that larger particles can be found closer to the inlet. Moreover, the growth rate of the chosen particles decreases gradually toward the outlet. A significant change is observed in the growth of the particle situated in the zone between 300 and 450 μm, which is due to the sedimentation of another particle close to the observed one.

For the sake of completeness, it has to be mentioned that because of the random nucleation, unusually large particles may form in the zones as, due to the perturbation upon nucleation, each calculation contains a random factor. Thus, in some cases, larger particles can also be found in zones that are far from the inlet, but the overall behavior of the particles in the bins is identical. Such a case is represented in Figure 6, where the cumulative curves of two zones (450−600 and 600−750 μm) are plotted in case of two calculations with identical parameters. Although the shapes of the curves are a good match with each other, there are two larger particles in the zone furthest from the inlet in the case of calculation No. 2. The two particles are exceptions from the characteristics of the zone.

The spatiotemporal behavior of the particles can be further investigated by exploring the spatial distribution of nucleation.

https://doi.org/10.1021/acs.cgd.3c00839
Cryst. Growth Des. 2023, 23, 8116−8123

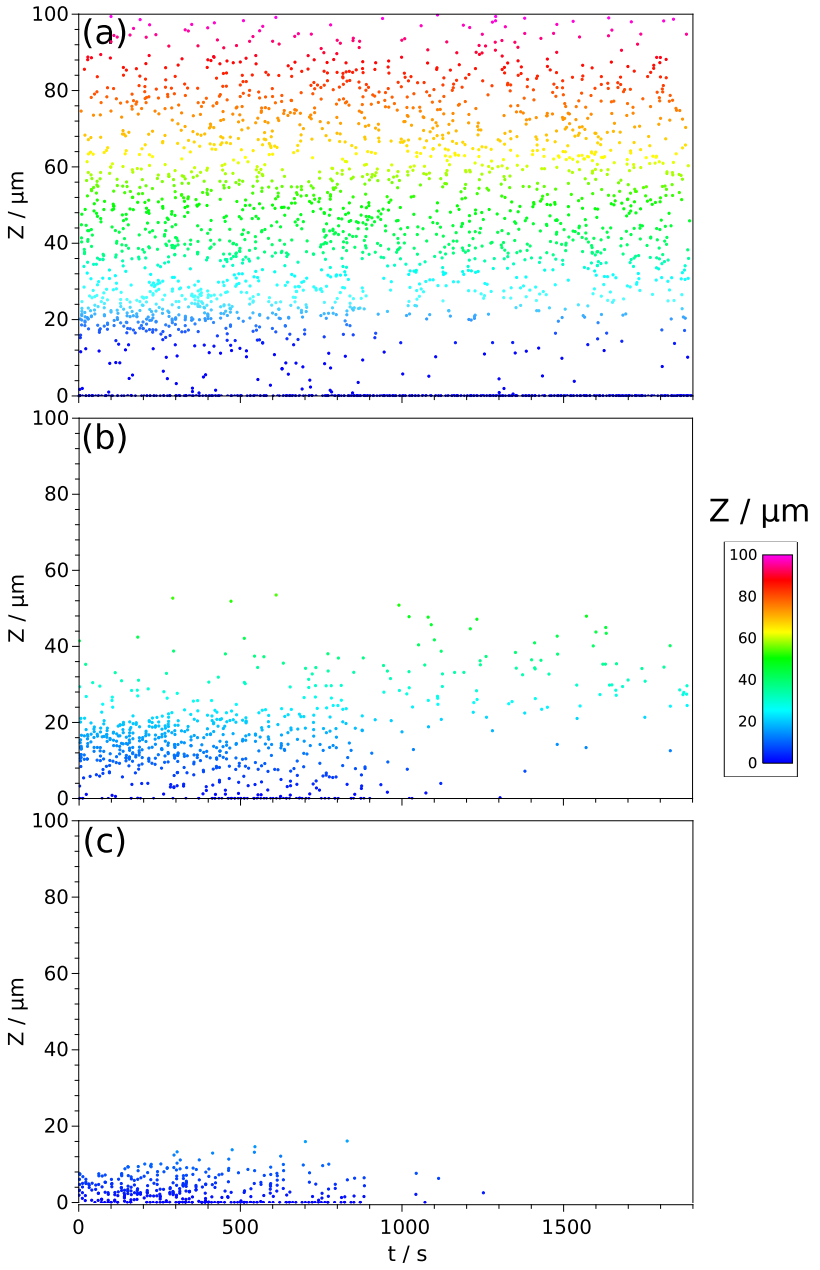

Figure 8. Temporal evolution of the nucleation sites for each particle that sediments in the following channel length intervals $0 < X \leq 5$ mm (a), 10 mm $< X \leq 15$ mm (b), and 20 mm $< X \leq 25$ mm (c) from the point of confluence.

In Figure 7, the time and location of nucleation sites are presented for particles that sediment in the channel.

The two coordinates X and Z denote the distance from the inlet and the channel height, respectively. At the beginning of the numerical experiments, particles nucleate everywhere in the channel independent of their position as the reactant solutions fill the reactor (cf. Figure 8). In the later stages, nucleation only close to the inlet and at the upper region of the reactor generates particles that sediment in the channel. Since nucleation and growth are two competing processes, at the lower regions, where the growth of sedimented particles is dominant, the criterium in eq 10 is never fulfilled; thus, nucleation only takes place at the top of the reactor. Further away from the point of confluence, the reactants are completely depleted due to the continuous growth of already existing particles.

CONCLUSIONS

In this work, we investigated the spatiotemporal precipitation of CaOx crystals in a reversible microchannel. The habits of the crystals were examined through careful imaging and statistical analysis of the precipitated crystals at different experimental times and positions in the microchannel. Our results show that upon mixing the reagents under laminar flow by interdiffusion, the size of the precipitated particles decreases from the inlet to the outlet of the microchannel following the changes in the supersaturation. With time, the polydispersity of the crystals becomes narrower, while the growth of each particle is dependent on the position in the channel. In addition, it allowed us to conclude that for COD crystals, the unstable phase is promoted by low supersaturation but steep reactant gradients. Our observations by numerical simulations reproduce the experimental results and suggest that nucleation

https://doi.org/10.1021/acs.cgd.3c00839
Cryst. Growth Des. 2023, 23, 8116−8123

occurs in the entire channel contrary to the growth, which seems to continue only with time for the crystals further from the point of confluence. We hope these results can help rationalize the formation of CaOx crystals in confined channels and shed light on processes observed in nature, such as in kidney stones.

AUTHOR INFORMATION

Corresponding Authors

Ali Abou-Hassan − *Sorbonne Université, CNRS UMR 8234, Laboratoire de PHysico-chimie des Électrolytes et Nanosystèmes InterfaciauX, PHENIX, F-75252 Paris, France; Institut Universitaire de France (IUF), 75231 Paris, France;* orcid.org/0000-0002-9070-1024; Email: ali.abou_hassan@sorbonne-universite.fr

Dezső Horváth − *Department of Applied and Environmental Chemistry, University of Szeged, Szeged H-6720, Hungary;* orcid.org/0000-0003-3852-6879; Email: horvathd@chem.u-szeged.hu

Authors

Paszkál Papp − *Department of Physical Chemistry and Materials Science, University of Szeged, Szeged H-6720, Hungary;* orcid.org/0000-0003-3608-4886

Samantha Bourg − *Sorbonne Université, CNRS UMR 8234, Laboratoire de PHysico-chimie des Électrolytes et Nanosystèmes InterfaciauX, PHENIX, F-75252 Paris, France*

Michael Emmanuel − *Department of Physical Chemistry and Materials Science, University of Szeged, Szeged H-6720, Hungary*

Ágota Tóth − *Department of Physical Chemistry and Materials Science, University of Szeged, Szeged H-6720, Hungary;* orcid.org/0000-0001-8254-6354

Complete contact information is available at: https://pubs.acs.org/10.1021/acs.cgd.3c00839

Notes

The authors declare no competing financial interest.

ACKNOWLEDGMENTS

This work has been supported by the National Research, Development and Innovation Office (K138844) and TKP2021-NVA-19 project. This work was also funded by Fondation de la Recherche Medicale (FRM, programme Chimie-Médecine 2018), which is greatly acknowledged. The authors would also like to thank Isabelle Génois (LCMCP, Sorbonne Université) for the SEM experiments. P.P. acknowledges the support by the New National Excellence Program of the Ministry for Culture and Innovation from the source of the National Research, Development and Innovation Fund (ÚNKP-22-3-SZTE-441). The authors thank the University of Szeged Open Access Fund (6568) for support.

REFERENCES

(1) Kaplan, C. N.; Noorduin, W. L.; Li, L.; Sadza, R.; Folkertsma, L.; Aizenberg, J.; Mahadevan, L. Controlled growth and form of precipitating microsculptures. *Science* **2017**, *355* (6332), 1395−1399, DOI: 10.1126/science.aah6350.

(2) He, H.; Chen, L.; Wang, Z.; Zhang, L.; Ge, T.; Xiang, X.; Wang, S.; Huang, Y.; Li, S. Screening the ion compositions on crystal morphology transitions by a microfluidic chip with a well-defined concentration gradient. *Cryst. Growth Des.* **2020**, *20*, 6877−6887.

(3) Bohner, B.; Schuszter, G.; Berkesi, O.; Horváth, D.; Tóth, Á. Self-organization of calcium oxalate by flow-driven precipitation. *Chem. Commun.* **2014**, *50* (33), 4289−4291, DOI: 10.1039/C4CC00205A.

(4) Bohner, B.; Endrődi, B.; Horváth, D.; Tóth, Á. Flow-driven pattern formation in the calcium-oxalate system. *J. Chem. Phys.* **2016**, *144* (16), No. 164504, DOI: 10.1063/1.4947141.

(5) Ibis, F.; Nuhu, M. A.; Penha, F. M.; Yu, T. W.; van der Heijden, A. E. D. M.; Kramer, H. J. M.; Eral, H. B. Role of hyaluronic acid on the nucleation kinetics of calcium oxalate hydrates in artificial urine quantified with droplet microfluidics. *Cryst. Growth Des.* **2022**, *22*, 3834−3844.

(6) Bazin, D.; Daudon, M.; Combes, C.; Rey, C. Characterization and some physicochemical aspects of pathological microcalcifications. *Chem. Rev.* **2012**, *112* (10), 5092−5120, DOI: 10.1021/cr200068d.

(7) Gay, C.; Letavernier, E.; Verpont, M.-C.; Walls, M.; Bazin, D.; Daudon, M.; Nassif, N.; Stéphan, O.; de Frutos, M. Nanoscale Analysis of Randall's Plaques by Electron Energy Loss Spectromicroscopy: Insight in early biomineral formation in human kidney. *ACS Nano* **2020**, *14*, 1823−1836.

(8) Kuliasha, C. A.; Rodriguez, D.; Lovett, A.; Gower, L. B. In situ flow cell platform for examining calcium oxalate and calcium phosphate crystallization on films of basement membrane extract in the presence of urinary 'inhibitors'. *CrystEngComm* **2020**, *22*, 1448−1458.

(9) Lovett, A. C.; Khan, S. R.; Gower, L. B. Development of a two-stage in vitro model system to investigate the mineralization mechanisms involved in idiopathic stone formation: stage 1—biomimetic Randall's plaque using decellularized porcine kidneys. *Urolithiasis* **2019**, *47*, 321−334.

(10) O'Kell, A. L.; Lovett, A. C.; Canales, B. K.; et al. Development of a two-stage model system to investigate the mineralization mechanisms involved in idiopathic stone formation: stage 2 in vivo studies of stone growth on biomimetic Randall's plaque. *Urolithiasis* **2019**, *47*, 335−346.

(11) Laffite, G.; Leroy, C.; Bonhomme, C.; Bonhomme-Coury, L.; Letavernier, E.; Daudon, M.; Frochot, V.; Haymann, J. P.; Rouzière, S.; Lucas, I. T.; Bazin, D.; Babonneau, F.; Abou-Hassan, A. Calcium oxalate precipitation by diffusion using laminar microfluidics: toward a biomimetic model of pathological microcalcifications. *Lab Chip* **2016**, *16*, 1157−1160.

(12) Rakotozandriny, K.; Bourg, S.; Papp, P.; Tóth, Á.; Horváth, D.; Lucas, I. T.; Babonneau, F.; Bonhomme, C.; Abou-Hassan, A. Investigating CaOx crystal formation in the absence and presence of polyphenols under microfluidic conditions in relation with nephrolithiasis. *Cryst. Growth Des.* **2020**, *20*, 7683−7693.

(13) Shim, J.-u.; Cristobal, G.; Link, D. R.; Thorsen, T.; Fraden, S. Using microfluidics to decouple nucleation and growth of protein crystals. *Cryst. Growth Des.* **2007**, *7*, 2192−2194.

(14) Zeng, Y.; Cao, J.; Wang, Z.; Guo, J.; Lu, J. Formation of amorphous calcium carbonate and its transformation mechanism to crystalline $CaCO_3$ in laminar microfluidics. *Cryst. Growth Des.* **2018**, *18*, 1710−1721.

(15) Sounart, T. L.; Safier, P. A.; Voigt, J. A.; Hoyt, J.; Tallant, D. R.; Matzke, C. M.; Michalske, T. A. Spatially-resolved analysis of nanoparticle nucleation and growth in a microfluidic reactor. *Lab Chip* **2007**, *7*, 908−915.

(16) Krishna, K. S.; Li, Y.; Li, S.; Kumar, C. S. S. R. Lab-on-a-chip synthesis of inorganic nanomaterials and quantum dots for biomedical applications. *Adv. Drug Delivery Rev.* **2013**, *65*, 1470−1495.

(17) Kotrly, S.; Šucha, L. *Handbook of Chemical Equilibria in Analytical Chemistry*; Ellis Horwood Ltd., 1985.

(18) Mullin, J. W. *Crystallization*; Butterworth-Heineman, 2001.

(19) Ananth, K.; Kavanagh, J. P.; Walton, R. C.; Rao, P. N. Enlargement of calcium oxalate stones to clinically significant size in an in-vitro stone generator. *BJU Int.* **2002**, *90*, 939−944.

(20) Weller, H. G.; Tabor, G.; Jasak, H.; Fureby, C. A tensorial approach to computational continuum mechanics using object-oriented techniques. *Comput. Phys.* **1998**, *12*, 620−631.

(21) Issa, R. I. Solution of the implicitly discretised fluid flow equations by operator-splitting. *J. Comput. Phys.* **1986**, *62*, 40−46.
(22) Raponi, A.; Romano, S.; Battaglia, G.; Buffo, A.; Vanni, M.; Cipollina, A.; Marchisio, D. Computational modeling of magnesium hydroxide precipitation and kinetics parameters identification. *Cryst. Growth Des.* **2023**, *23*, 4748−4759.
(23) Emmanuel, M.; Horváth, D.; Tóth, Á. Flow-driven crystal growth of lithium phosphate in microchannels. *CrystEngComm* **2020**, *22*, 4887−4893.
(24) Haider, A.; Levenspiel, O. Drag coefficient and terminal velocity of spherical and nonspherical particles. *Powder Technol.* **1989**, *58*, 63−70.

https://doi.org/10.1021/acs.cgd.3c00839
Cryst. Growth Des. 2023, 23, 8116−8123